A Consistent Explanation for the Unusual Initial Mass Function and Star Formation Rate in the Central Molecular Zone (CMZ)

Gilles Chabrier, Pierre Dumond

The Astrophysical Journal, 966:48 (12pp), 2024 May 1 https://doi.org/10.3847/1538-4357/ad33c0

A Consistent Explanation for the Unusual Initial Mass Function and Star Formation Rate in the Central Molecular Zone (CMZ)

Gilles Chabrier[1,2] and Pierre Dumond[1]
[1] Ecole normale supérieure de Lyon, CRAL, Université de Lyon, UMR CNRS 5574, F-69364 Lyon Cedex 07, France; chabrier@ens-lyon.fr, pierre.dumond@ens-lyon.fr
[2] School of Physics, University of Exeter, Exeter, EX4 4QL, UK
Received 2024 January 10; revised 2024 February 29; accepted 2024 March 11; published 2024 April 25

Abstract

We examine various physical processes that may explain the shallow high-mass slope of the initial mass function (IMF), as well as the low star formation rate (SFR) in star-forming molecular clouds (MCs) in the Central Molecular Zone (CMZ). We show that the strong tidal field and shear experienced by the CMZ have opposite effects on the collapse of density fluctuations and cannot explain these properties. Similarly, we show that the intense magnetic field in the CMZ provides a negligible pressure support and, for the high densities at play, should not modify the probability density function of the turbulent gas flow, thus affecting negligibly the IMF. However, we show that, in contrast to the MCs in the Galactic disk, the ones in the CMZ experience only one single episode of turbulence cascade. Indeed, their rather short lifetime, due to their high mean densities, is similar to one typical turbulence crossing time. Consequently, according to the Hennebelle–Chabrier theory of star formation, within this "single turbulence cascade episode," the cloud experiences one single field of turbulence-induced density fluctuations, leading eventually to gravitationally unstable cores. As shown in Hennebelle & Chabrier (2013), this yields a shallower IMF than usual and leads to the correct observed slope for the CMZ star-forming clouds. Similarly, this single large-scale turbulence event within the cloud lifetime yields a 5–6 times lower SFR than under usual conditions, in agreement with the observed values. Therefore, we suggest that this "single turbulence cascade" scenario can explain both the shallow IMF and low SFR of clouds in the CMZ.

Unified Astronomy Thesaurus concepts: Milky Way Galaxy (1054)

1. Introduction

The Central Molecular Zone (CMZ), i.e., the region within a Galactocentric radius $R \simeq 300$ pc, hosts several young massive clusters, including the young nuclear cluster (YNC; ~2.5–5.8 Myr, $M \geqslant 2 \times 10^4\,M_\odot$; Lu et al. 2013) and the Arches cluster (~2–4 Myr, $M \sim 4$–$6 \times 10^4\,M_\odot$; Lohr et al. 2018), characterized by an unusual stellar initial mass function (IMF) compared with the canonical IMF, which is usually found to exhibit very little variation in various environments. Indeed, the slopes of these IMFs, $\mathcal{N}(M) = dN/dM \propto M^{-\alpha}$, have been found to be significantly flatter than the usual Salpeter slope ($\alpha = 2.35$), with $\alpha = 1.7 \pm 0.2$ for the YNC (Lu et al. 2013) and $\alpha = 1.80^{0.05}_{0.05}$–$2.0^{0.14}_{0.19}$ for the Arches cluster, depending on the functional form fitted, with potentially a strong steepening above ~4–8 $M_\odot$ (Hosek et al. 2019). The same behavior, with $\alpha = 1.68^{0.13}_{0.09}$, has been found for the Quintuplet cluster (Hußmann et al. 2012), although it is unclear whether or not this is due to mass segregation for this slightly older cluster. Other Galactic clusters might have slopes consistent with that seen in the Arches cluster (e.g., Wd1, NGC 3603; Lim et al. 2013; Pang et al. 2013; Andersen et al. 2017; Lu et al. 2020), although these results are more uncertain. There is also tentative evidence that this shallow mass function is also present for the prestellar cores, with an apparent excess of high-mass sources, even though substantial uncertainties remain in these measurements (Lu et al. 2020; Henshaw et al. 2023).

Furthermore, the mean value of the star formation rate (SFR) in the CMZ is found to be about $0.07^{0.08}_{0.02}\,M_\odot\ \mathrm{yr}^{-1}$, significantly below the Kennicutt–Schmidt relation for its gas surface density and about an order of magnitude below Lada's relationship (Lada et al. 2012) between the SFR and the mass of dense, molecular gas, a relationship that holds for nearby molecular clouds (MCs) as well as for external galaxies (Longmore et al. 2013; Hosek et al. 2019). It is not clear yet, however, whether this low SFR for the amount of dense gas is also found for the CMZs of external galaxies or only for the Galactic CMZ. Numerous studies have been devoted to the unusual SFR of the CMZ, invoking, in particular, feedback radiation or Galactic shear to explain its lower-than-expected value (see Henshaw et al. 2023), with no real conclusive explanation. To the best of our knowledge, however, only one study has been devoted to the puzzle of the top-heavy, shallow IMF of the CMZ clusters, though only through numerical simulations (Dib et al. 2007).

In this paper, we examine both issues, IMF and SFR, throughout an analytical exploration of the various physical processes that could be responsible for these CMZ particular properties. The paper is organized as follows. In Section 2, we summarize the thermodynamic and dynamical properties of the CMZ. In Section 3, we recall the various relevant scaling properties for star-forming MCs. In Sections 4 and 5, we derive the equations allowing us to characterize the impact of the Galactic tidal field and shear on the IMF, respectively. In Section 6, we examine the dynamics of the star formation process in the CMZ and explore the consequences for both the IMF and the SFR. Section 7 is devoted to the conclusion.

2. Properties of the Central Molecular Zone

A recent summary of the properties of the CMZ can be found in the review of Henshaw et al. (2023). The conditions in the CMZ are extreme compared with the solar neighborhood and comparable to those found in the early universe (e.g., Kruijssen & Longmore 2013). The part where most of the molecular gas is located, $45 \lesssim r/\mathrm{pc} \lesssim 115$, denoted the gas stream, includes all the major cloud complexes in the Galactic center (GC).

The molecular gas in the CMZ is distributed along an approximately ringlike, or possibly a more torus-like, structure (Kruijssen et al. 2015), and thus follows eccentric orbits. This gas exhibits velocity dispersions much larger than those measured in Galactic disk clouds, indicating a much higher level of turbulence, as found in extreme environments. Various mechanisms can be responsible for injecting such amounts of large-scale turbulence, a point we will examine in more detail in Section 6.2.

The properties of the CMZ are the following (Henshaw et al. 2023). The temperature ranges from about 50 to 100 K, which yields a typical sound speed $C_S \simeq 0.4$–0.6 km s^{-1}. The scale dependence of the mean density of MCs in the CMZ can be inferred from the determinations of Tanaka et al. (2020) and Krieger et al. (2020):

$$M = M_0 \left(\frac{R}{1\ \mathrm{pc}}\right)^{2.7} M_\odot \Longrightarrow \bar{n} = n_0 \left(\frac{R}{1\ \mathrm{pc}}\right)^{-0.3} \mathrm{cm}^{-3}. \quad (1)$$

However, while the first authors suggest $M_0 = 10^{3.5}\, M_\odot$, yielding $n_0 = 6 \times 10^4\, \mathrm{cm}^{-3}$, the second group gets $M_0 = 200\, M_\odot$, and then $n_0 = 3.8 \times 10^3\, \mathrm{cm}^{-3}$. Typical sizes for star-forming MCs in the CMZ are $L_c \sim 1$–10 pc. The scaling properties of the 3D rms velocity slightly differ from the usual Larson relation, with

$$V_{\rm rms}(R) \equiv V^{\rm 3D}_{\rm rms}(R) = \sqrt{3}\, V^{\rm 1D}_{\rm rms}(R) = \sqrt{3}\, V_0 \times \left(\frac{R}{1\ \mathrm{pc}}\right)^{\eta}, \quad (2)$$

where V_0 is the 1D observational determination along the line of sight. Whereas the power index $\eta \simeq 0.7$ is found in most studies, the observationally determined normalization at 1 pc differs substantially. It should be stressed, however, that these determinations do not probe the same scales! Using tracers CO (3–2) and CO (1–0) from 1 to 100 pc, Krieger et al. (2020) find a value $V_0 = 2$ km s^{-1}. At smaller scales, in the range 0.1–1 pc, Tanaka et al. (2020), using HCN as a tracer, find $V_0 = 10$ km s^{-1}. At even smaller scales, Henshaw et al. (2019), using a different method to determine the velocity dispersion, find an even larger value for the Brick, $V_0(0.07\ \mathrm{pc}) = 4.4 \pm 2.2$ km s^{-1}, substantially higher than extrapolations from the above larger-scale determinations. Thus, there seems to be an increase of the observed velocity dispersion normalization with decreasing scale. It is worth noting that while 1–100 pc scales are relevant for cloud scales, the smaller ($\lesssim$1 pc) scales are more representative of core scales. As will be discussed later, it is important to take into consideration this difference of scales in the observational determination of the velocity dispersion, depending on whether one considers clouds or prestellar cores, which is the case for the IMF/core mass function (CMF). We will come back to the issue in Section 5.1. In the study of Federrath et al. (2016), devoted to one of the CMZ clouds, the turbulence appears to be purely solenoidal, implying a factor $b \simeq 1/3$ or even $b = 0.2$ for the turbulence driving parameter, a consequence of the strong shear. This does not imply, however, that this dominant solenoidal nature of turbulence applies to all clouds in the CMZ.

Using Equations (1) and (2), we can determine a few typical mean quantities for the CMZ (taking a fiducial value $\bar{n} = 10^4\, \mathrm{cm}^{-3}$), notably the Jeans length, $\lambda_{\rm J} = \sqrt{C_s/G\bar{\rho}} \simeq$ 0.4–0.6 pc, and Jeans mass, $M_{\rm J} = (4\pi/3)\lambda_{\rm J}^3 \bar{\rho} \approx 50$–$150\ M_\odot$. The typical 3D rms Mach number at the injection scale ($L_i \simeq L_c$ for the star-forming clouds) lies in the range $\mathcal{M} = \sqrt{3}\frac{V_0}{C_s}\left(\frac{L_i}{1\ \mathrm{pc}}\right)^{\eta} \approx 8$–$170$, depending on the chosen 1 pc normalization value. This yields cloud typical turbulent crossing time and sonic length:

$$\tau_{ct} \simeq \frac{L_c}{V^{\rm 1D}_{\rm rms}(L_c)} \approx 0.2\text{–}2\ \mathrm{Myr} \quad \text{for} \quad L_c \sim 1\text{–}10\ \mathrm{pc} \quad (3)$$

$$l_s = \left(\frac{C_s}{V_0}\right)^{1/\eta} = \mathcal{M}^{-1/\eta}\, L_c \approx 0.01\text{–}0.1\ \mathrm{pc}. \quad (4)$$

3. The Slope of the IMF

3.1. Impact of the Velocity–Size Relation

In the general gravoturbulent scenario of star formation (Padoan & Nordlund 2002; Hennebelle & Chabrier 2008; Hopkins 2012), density fluctuations in MCs are due to the shock cascade of large-scale compressible turbulence characterized by a log-density power spectrum $\mathcal{P}(\delta) \propto k^{-n}$, where $\delta = \log(\rho/\bar{\rho})$, with a typical 3D index found to be very similar to the one found for the velocity, $n \simeq 3.8$ (Beresnyak et al. 2005). The variance of the dispersion of the log-density field generated by turbulence at scale R is taken to be (Hennebelle & Chabrier 2008, hereafter HC08)

$$\sigma^2(R) = \sigma_0^2 \left[1 - \left(\frac{R}{L_i}\right)^{n-3}\right]. \quad (5)$$

The variance at small (core) scale ($R \ll L_c$), which is what really matters for the IMF, is found in hydrodynamical and MHD simulations to be reasonably well described under some conditions by the relation (Molina et al. 2012)

$$\sigma_0^2 = \ln\left[1 + (b\mathcal{M})^2 \left(\frac{\beta}{1+\beta}\right)\right], \quad (6)$$

where $\beta = 2(\mathcal{M}_{\rm A}/\mathcal{M})^2$ and $\mathcal{M}_{\rm A} = V_{\rm rms}/V_{\rm A}$ is the 3D rms Alfvenic Mach number, where $V_{\rm A} = B_{\rm 3D}/\sqrt{\mu_0 \bar{\rho}}$ denotes the 3D mean Alfvén velocity, with μ_0 the permeability of vacuum.

In the canonical Hennebelle & Chabrier theory of the IMF (Equation (29) of HC08), the collapsing barrier for the density fluctuations of scale R generated by turbulence reads

$$e^{s_R^c} = \frac{\rho_R^c}{\bar{\rho}} \geqslant \tilde{R}(1 + \mathcal{M}_\star^2 \tilde{R}^{2\eta}), \quad (7)$$

which yields for the dominant term in the IMF

$$\mathcal{N}(M_R^c) = \frac{dN}{d\tilde{M}_R^c} \propto \frac{1}{\tilde{M}_R^c} \frac{de^{s_R^c}}{d\tilde{R}} \frac{d\tilde{R}}{d\tilde{M}_R^c} \mathcal{P}(e^{s_R^c}), \quad (8)$$

where $\tilde{R} = R/\lambda_J$ and $\tilde{M} = M/M_J$ are normalized to the Jeans length and the Jeans mass, respectively. $\mathcal{M}_\star = \frac{\mathcal{M}}{\sqrt{3}}\left(\frac{\lambda_J}{L_i}\right)^\eta \simeq (\frac{\lambda_J}{1\,\mathrm{pc}})(\frac{V_0}{C_S}) \approx 2$ and $\sim$10 for Krieger et al. (2020) and Tanaka et al. (2020) 1 pc normalizations, respectively, is the Mach number at the Jeans scale. In the time-dependent extension of the theory (Equation (21) of Hennebelle & Chabrier 2013, hereafter HC13), the slope of the high-mass tail of the IMF is given by

$$\alpha = \frac{4+2\eta}{2\eta+1} + 6\frac{\eta-1}{(2\eta+1)^2}\frac{\ln(\mathcal{M}_\star)}{\sigma^2}. \tag{9}$$

One can already notice that, because of the larger-than-usual Larson turbulent index $\eta = 0.7$ (instead of $\eta \approx 0.5$), the first term in Equation (5) yields a shallower slope than the one predicted in the solar neighborhood by a factor $\sim$0.25, while, under the present conditions, the second term amounts to about -0.1. This flattening reflects the high gas dispersion due to more vigorous turbulence, which prevents large-scale star-forming clumps from collapsing (Chabrier & Hennebelle 2011). Then, although contributing to the flattening of the high-mass tail of the IMF, this modification of the velocity–size relation of turbulence is not sufficient to explain the aforementioned observed values of α.

3.2. Impact of Gravity on the Probability Density Function

It must be remembered that the HC theory is based on the assumption of a purely lognormal probability density function (pdf) in MCs. There is ample observational evidence, however, that the pdf of star-forming clouds develops a power law at high density, due to the onset of gravity, and thus cannot be entirely described by a lognormal form (e.g., Schneider et al. 2022). Recently, Jaupart & Chabrier (2020) developed a predictive analytical theory to characterize the impact of gravity on the pdf of turbulence. They demonstrated that the power law will start to develop above a critical density $s_{\rm crit} = \log(\rho_{\rm crit}/\bar{\rho})$ given by the condition

$$e^{s_{\rm crit}} = \frac{45b^2\mathcal{M}_\star^2}{\pi\sigma_0^2}\left(s + \frac{1}{2}\sigma_0^2\right), \tag{10}$$

assuming that σ_0 weakly depends on scale. This yields $s_{\rm crit} \simeq 9$ for the value of V_0 obtained by Tanaka et al. (2020) and $s_{\rm crit} \simeq 5$ for the value derived by Krieger et al. (2020). The fact that no (or a quite small) power law is observed in the pdf of MCs of the CMZ (Henshaw et al. 2023) suggests that V_0 should be close to the first value. This is also consistent with the higher velocity amplitude suggested by Henshaw et al. (2019) for the Brick. The Jaupart–Chabrier formalism thus shows that the power law in the pdf of the CMZ will develop at a higher density (or later for a given high enough density) than for standard Milky Way MCs, highlighting again the vigorous level of turbulence in these regions.

3.3. Impact of the Magnetic Field

The magnetic field in the CMZ ranges from about 10 to 1000 μG, a much stronger value than in the solar neighborhood (Henshaw et al. 2023; Lu et al. 2024). It is generally admitted that at high density the amplitude of the magnetic field scales as $B \propto \rho^{n_B}$, with n_B varying from 1/2 to 0 at very high density, where it saturates. We examine both cases below.

In the case $n_B = 1/2$, the magnetic energy in the virial equation does not depend on the scale, so we simply need to rescale the Jeans length as

$$C_s' \rightarrow (C_s^2 + V_{\rm A}^2)^{1/2};\ \ \lambda_{\rm J}^B = \frac{C_s'}{\sqrt{G\bar{\rho}}};\ \ \mathcal{M}_\star = \frac{1}{\sqrt{3}}\frac{V_0}{C_s'}\left(\frac{\lambda_{\rm J}^B}{1\,\mathrm{pc}}\right)^{2\eta}, \tag{11}$$

where $V_{\rm A} = B/\sqrt{\mu_0\bar{\rho}} \sim 1\ \mathrm{km\ s^{-1}}$.

In the case $n_B = 0$, the impact of the magnetic field pressure can be taken into account by rescaling $\mathcal{M}_\star$ (see Section 2.3.1 of HC13):

$$\mathcal{M}_\star^2 \rightarrow \frac{\mathcal{M}_\star^2}{2}\left(1 + \sqrt{1 + \frac{4V_{\rm A}^{\star\,2}}{\mathcal{M}_\star^4}}\right) \tag{12}$$

$$\text{with } V_{\rm A}^\star = \frac{1}{\sqrt{6}}\frac{V_A}{C_s} = \frac{1}{\sqrt{6}}\frac{\mathcal{M}}{\mathcal{M}_{\rm A}}. \tag{13}$$

The collapsing barrier is the same as in Equation (7) with the rescaled value of $\mathcal{M}_\star$.

Typical CMZ conditions yield $\mathcal{M}_{\rm A} \sim 30$, $V_{\rm A}^\star \sim 1$. For the velocity dispersions of Tanaka et al. (2020), the correction on $\mathcal{M}_\star$, and thus on the slope, is found to be negligible. For the smaller value of Krieger et al. (2020), the correction on the slope is $\sim$0.05. In all cases, the impact of the magnetic field pressure on the slope of the IMF is found to be too small to explain the flattening of the high-mass tail of the IMF.

It is interesting to estimate the magnetic field that would be necessary to explain the flattening of the high-mass slope of the IMF, $\Delta\alpha \sim 0.6$ (see Section 1). Using Equation (5), the slope difference between the magnetized and nonmagnetized ($B = 0$) cases is

$$\alpha_B - \alpha_{B=0} = \frac{6(\eta-1)}{(2\eta+1)^2\sigma^2}\ln\left(\frac{\mathcal{M}_\star}{\mathcal{M}_\star^{B=0}}\right) \approx -\frac{0.3}{\sigma^2}\ln\left(\frac{\mathcal{M}_\star}{\mathcal{M}_\star^{B=0}}\right). \tag{14}$$

Picking the most favorable case, i.e., a small (1 pc), moderately turbulent (Krieger et al. 2020; rms velocity normalization) cloud, for the magnetic pressure to provide sufficient support to explain the slope of the IMF, the magnetic field should be about 3 orders of magnitude larger than the upper limit of the aforementioned observed values. Using the velocity normalization of Tanaka et al. (2020), the field would need to be at least 5 orders of magnitude larger than this upper value.

However, depending on its dependence on density, the magnetic field can modify or not the pdf of the turbulence in the star-forming gas. In the case $n_B = 1/2$, the magnetic field yields a narrower variance than in the purely hydrodynamical case, as seen from Equation (6). Recent observations (Lu et al. 2024) have allowed us to infer the turbulent component of the magnetic field, B_t, in some clouds of the CMZ, $V_{\rm A,rms} \equiv V_{{\rm A},t} = (\langle B_t^2\rangle/\langle B_{\rm tot}^2\rangle)^{1/2}V_{\rm A,tot}$. Using their Table 1, we get typical values of the rms Alfvenic velocity $V_{\rm A,rms} \approx$ 1–3 km s^{-1} and rms Alfvenic Mach numbers $\mathcal{M}_{\rm A} \approx$ 20–40. This yields $\beta \approx 0.1$–0.5. These values are consistent with the results of the numerical simulations of Federrath et al. (2016). In that case, we have verified that the modification of the pdf of

the gas due to the strong turbulent magnetic field flattens significantly the slope of the IMF and potentially yields values consistent with the observed value. This will be illustrated later on in Section 6.1. As will be seen, however, this depends on the chosen value of the field at core scales, a quantity very difficult to determine precisely.

However, a case $n_B = 1/2$ in the magnetic field–density dependence is probably not realistic for the high densities typical of the CMZ clouds ($\bar{n} \gtrsim 10^4$ cm^{-3}). At such densities, the gas and the magnetic field are decoupled and the shock continuity equation is independent of the magnetic field strength, yielding $n_B \simeq 0$ (Molina et al. 2012). In that case, we recover the nonmagnetic, hydrodynamical regime ($\beta \rightarrow \infty$), and the density variance in Equation (6) simply becomes $\sigma_0^2 = \ln[1 + (b\mathcal{M})^2]$ (Padoan et al. 1997).

4. The Tidal Field

Due to its central Galactic location, the CMZ experiences the strong impact of the Galactic tidal field. The spherically symmetric, enclosed mass distribution over the range $R = 1$–300 pc has been derived by Launhardt et al. (2002). The inferred mass profile has been shown by Kruijssen et al. (2015) to be well modeled by a power law $M(r) \propto r^{\xi}$ with $\xi = 2.2$ in the region $45 < r/\mathrm{pc} < 115$ (solid-body rotation corresponds to $\xi = 3$), which matches the radial extent of the gas stream, where the star-forming clouds are located. The fact that $\xi > 2$ implies that all the components of the tidal tensor are compressible. The complete derivation of the equations is given in Appendix A. As shown in this appendix, the global collapse condition for an ellipsoidal overdensity $\rho_R/\bar{\rho}$ of scale R in the presence of a tidal field becomes $e^{s_R} \geqslant e^{s_R^c}$, with

$$e^{s_R^c} = \frac{2}{I}\frac{1}{\tilde{c}^2}\left[(1 + \mathcal{M}_\star^2 \tilde{a}^{2\eta}) - \frac{\mu}{15}\tilde{c}^2\left((\xi - 2) + \frac{\tilde{b}^2}{\tilde{c}^2} + \frac{\tilde{a}^2}{q_\phi^2 \tilde{c}^2}\right)\right], \tag{15}$$

where $\tilde{a}$, $\tilde{b}$, $\tilde{c}$ are the semiaxis of the ellipsoidal cloud, with $\tilde{a}$ its longest length, normalized to the Jeans length; I is the normalized deformation tensor; $\mu = M(r_0)/\bar{\rho} r_0^3 \simeq 0.08$ at $r_0 = 100$ pc is the tidal factor; and q_ϕ produces a potential flattened in the z-direction ($q_\phi = 1$ corresponds to a spherically symmetric potential). The best-fitting value to the orbital parameters of the observed clouds yields $q_\phi = 0.63$ (Dale et al. 2019). The first term in the brackets of Equation (A11) is the usual HC08 barrier (see Equation (7)) while the second term is the tidal contribution. Assuming, for sake of simplicity, that the turbulence-induced perturbations remain nearly spherical ($a = b = c$), the threshold collapse density becomes

$$e^{s_R^c} = \frac{\rho_R^c}{\bar{\rho}} = \frac{1 + \mathcal{M}_\star^2 \tilde{R}^{2\eta}}{\tilde{R}^2} - \mu\kappa, \tag{16}$$

$$\Leftrightarrow \tilde{M}_R^c \approx \rho_R^c \tilde{R}^3 = \tilde{R}(1 + \mathcal{M}_\star^2 \tilde{R}^{2\eta}) - \tilde{R}^3 \mu\kappa, \tag{17}$$

where $\kappa = ((\xi - 2) + 1 + q_\phi^{-2})/15 \simeq 0.22$. We see that the collapsing barrier is decreased uniformly by the tidal field by a very small factor, $\mu\kappa \approx 0.02$ for the relevant parameter values. The tidal field thus (slightly) favors collapse.

Although the tidal parameter is very small, it is nevertheless interesting to examine its impact on the slope of the CMF. Indeed, one can imagine that the role of the tides might be increased by more complicated nonaxisymmetric mass distribution in the CMZ. Since the collapse barrier is decreased compared with the usual one, we need to verify that the condition below is fullfilled:

$$\frac{\rho_R^c}{\bar{\rho}} = e^{s_R^c} = \frac{1 + \mathcal{M}_\star^2 R^{2\eta}}{R^2} - \mu\kappa > 1. \tag{18}$$

This introduces a maximum scale R_1 for collapse:

$$\tilde{R} \leqslant \tilde{R}_1 \simeq \left(\frac{\mathcal{M}_\star^2}{1 + \mu\kappa}\right)^{\frac{1}{2-2\eta}} \approx M_\star^{3.3}. \tag{19}$$

Furthermore, as seen from Equation (17), the mass–size relation is no longer monotonic. This implies one more condition for collapse and thus another specific scale $\tilde{R}_2$:

$$\frac{d\tilde{M}_R^c}{d\tilde{R}} \geqslant 0 \Rightarrow 1 + \mathcal{M}_\star^2(2\eta + 1)\tilde{R}^{2\eta} - 3\mu\kappa\tilde{R}^2 \geqslant 0. \tag{20}$$

For $\tilde{R}_2 \leqslant \tilde{R}_1$, $d\tilde{M}_R^c/d\tilde{R} > 0$, $\tilde{M}_R^c$ decreases with $\tilde{R}$, and the clump will keep being gravitationally unstable, whereas in the opposite case a clump with a density above the threshold value may eventually become stable again after its initial collapse. Since we are interested in the large scales of the IMF, $\tilde{R} \gg 1$, we can estimate the maximum scale for pursuing collapse, $\tilde{R}_2$, as

$$\tilde{R} \leqslant \tilde{R}_2 \simeq \left(\frac{(2\eta + 1)\mathcal{M}_\star^2}{3\mu\kappa}\right)^{\frac{1}{2-2\eta}} \approx 370\, \mathcal{M}_\star^{3.3}. \tag{21}$$

It is easy to verify that, under the present conditions, $\tilde{R}_2/\tilde{R}_1 \approx 2/3\mu\kappa \gg 1$. Therefore, if condition (16) is fullfilled, so is condition (21). A case $\tilde{R}_2 < \tilde{R}_1$ would imply $\mu\kappa \gtrsim (2\eta + 1)/(2 - 2\eta) \approx 4$. Under such conditions, tidal effects could stabilize initially gravitationally unstable density fluctuations, modifying drastically the formation of prestellar cores. Given the relevant values of μ for the CMZ, however, such a regime does not occur in this region.

It is not simple to compute the exact dependence of the density on the critical mass under the combined action of turbulence and tides. However, we can approximate $\tilde{M} \propto \tilde{R}^{\gamma}$ with $\gamma \simeq 2\eta + 1 \simeq 2$ when turbulence dominates over tidal effects (see HC08) and $\gamma \rightarrow 0$ when $\tilde{R} \rightarrow \tilde{R}_2$ (since $d\tilde{M}_R^c/d\tilde{R} = 0$ for this scale). Thus, the dominant term in the expression of the IMF scales as (Equation (5))

$$\tilde{M}\mathcal{N}(\tilde{M}) = \frac{dN}{d\log \tilde{M}_R} \propto \tilde{M}_R^{-(\alpha-1)} \tag{22}$$

$$\propto \frac{de^{s_R^c}}{d\tilde{R}}\frac{d\tilde{R}}{d\tilde{M}} \tag{23}$$

$$\propto \tilde{M}^{-1-\frac{2}{\gamma}(1-\eta)}. \tag{24}$$

Note that the first derivative, $de^{s_R^c}/d\tilde{R}$, is not impacted by the tidal contribution since the term modifying the usual barrier does not depend on R. As $\gamma \rightarrow 0$, the slope of the IMF becomes steeper and steeper, as expected since the tidal field favors the collapse, as mentioned above. It is interesting to note, at this stage, that for clump sizes $R \gtrsim 1$ pc, Tanaka et al. (2020, their

Figure 3) derive a much steeper mass–size relation, $\tilde{M} \propto \tilde{R}^{\delta}$, with $\delta \simeq 2.7$. Assuming that these clumps are approximately in equilibrium, this corresponds to a barrier $\rho \propto R^{\delta-3} = R^{-0.3}$. The dominant term in the expression of the IMF thus becomes $\tilde{M}\mathcal{N}(\tilde{M}) \propto \tilde{M}^{-3/\delta} \propto \tilde{M}^{-1.1}$, flattening the high-mass slope of the IMF, but in any case still steeper than the observed slope. As mentioned earlier, however, the aforementioned scales are more characteristic of clouds than cores. For the latter typical scales ($\lesssim$1 pc), Tanaka et al. (2020) recover a value $\delta \simeq 1.6$, in agreement with our above estimate $0 \lesssim \gamma \lesssim 2$.

In summary, the tidal field slightly *steepens* the slope of the IMF compared with the usual Salpeter value. As mentioned previously, the main reason for this small impact of tidal interactions is the high compressibility of the tidal field for the inferred potential of the CMZ.

5. The Galactic Shear

Because it is located near the GC, the CMZ is also subject to a strong shear. The role of the shear has been suggested in many studies to explain the low SFR in the CMZ (e.g., Krumholz & Kruijssen 2015; Krumholz et al. 2017; Colling et al. 2018; Henshaw et al. 2023, and references therein). The impact of the shear on the IMF, however, has never been studied in detail (see, however, Dib et al. 2012 for a study on the observational side).

This impact is twofold. First, it contributes to the velocity dispersion. Second, it distorts the shape of the star-forming clumps. We examine both effects in detail.

5.1. The Shear as a Source of Velocity Dispersion

The calculations of the impact of the shear on the velocity dispersion are detailed in Appendix B. As mentioned in Section 2, the CMZ velocity dispersion seems to be well described by the Larson relation, although with an exponent ($\eta \simeq 0.7$) larger than the usual value ($\eta \simeq 0.5$). This reflects the fact that the shear gradient contributes to the velocity dispersion, besides turbulence (se,e e.g., Kruijssen et al. 2019). It must be kept in mind that observations are done along a line of sight, so the observed velocity dispersion is the 1D total velocity dispersion:

$$V_{1D} = \sqrt{(V_{1D}^{\rm shear})^2 + (V_{1D}^{\rm turb})^2}\,, \tag{25}$$

where (see Equation (B6))

$$V^{\rm shear} = \frac{3-\xi}{2}\sqrt{\frac{GM(r)}{r^3}}R = 0.7\left(\frac{R}{1{\rm pc}}\right){\rm km\ s^{-1}}, \tag{26}$$

where $\xi = 2.2$ is the coefficient of the enclosed mass distribution $M(r) \propto r^{\xi}$ determined from the gravitational potential of the CMZ, with $M = 5 \times 10^8 M_{\odot}$ at $r = 90$ pc (Kruijssen et al. 2019). Here we have used the value of the velocity normalization at 1 pc of Krieger et al. (2020), $V_0 = 2\ {\rm km\ s^{-1}}$. Indeed, as mentioned previously, this value has been determined in the range 1–100 pc, whereas the observations of Tanaka et al. (2020) concern the smaller scales ($\leqslant$1 pc), where the shear becomes negligible. The turbulent velocity dispersion scales as $V^{\rm turb} \propto R_{\rm turb}^{\eta}$, with $\eta_{\rm turb} \simeq 0.5$ for Burger's like turbulence, while $V^{\rm shear} \propto R$. The turbulent dispersion velocity at 1 pc is thus given by

$$V_{1D}^{\rm turb}(1{\rm pc}) = \sqrt{V_{1D}^2(1{\rm pc}) - (V^{\rm shear})^2(1\ {\rm pc})} \simeq 1.6\ {\rm km\ s^{-1}}. \tag{27}$$

Using a value $\eta_{\rm turb} \simeq 0.5$ for the index of turbulence,

$$V_{1D}^{\rm turb} = 1.6\left(\frac{R}{1\ {\rm pc}}\right)^{\eta_{\rm turb}}\ {\rm km\ s^{-1}}, \tag{28}$$

the scale at which the shear-induced motions will start to dominate the turbulent ones is given by

$$R_{\rm shear} = \left(\frac{V_{1{\rm pc}}^{\rm turb}}{V_{1{\rm pc}}^{\rm sh}}\right)^{\frac{1}{1-\eta_{\rm turb}}}\ {\rm pc} \simeq 5\ {\rm pc}. \tag{29}$$

This result is consistent with the value of 8 pc above which Federrath et al. (2016) show that the shear dominates the turbulent motions for the Brick cloud. These authors, however, supposed in their study that the shear leads to a 3D dispersion velocity, whereas the shear yields essentially 1D motions. This assumption increases the role of the shear. Since at large scales turbulence is isotropic, the turbulent velocity dispersion dominates the total 3D velocity dispersion over a much broader range of scale. Because of the $\sqrt{3}$ correction for $V_{3D}^{\rm turb}$ in Equation (29), in reality the shear dominates the turbulent dispersion only for $R \gtrsim 15$ pc. The predicted scalings of the 1D and 3D velocity dispersions are plotted in Figure 1. According to Equation (1), the shear will thus affect the formation of large MCs, for $M \gtrsim 10^5\ M_{\odot}$. This is consistent with the study of Jeffreson et al. (2018): these authors suggest that while at large ($R \gtrsim 100$ pc) and small ($R \lesssim 45$ pc) galactocentric radii the cloud lifetime in the CMZ is dominated by galactic shear, cloud evolution in the zone in between, which corresponds to the region of compressible tidal field, is dominated by dynamically compressive mechanisms. Consequently, clouds at short and large galactocentric distances are expected to be sheared apart before collapse.

Therefore, at the $\lesssim$10 pc scale, i.e., for the star-forming clouds, the shear plays no or a modest role because the medium is very dense. It might affect indirectly the mean SFR of the whole CMZ—since fewer clouds are formed, fewer stars are formed—but not the very star formation process, and thus the IMF. Therefore, at these scales, we should expect the exponent of the velocity–size relation to be $\eta \simeq 0.5$, the usual Larson coefficient characteristic of the compressible turbulence cascade, instead of the observed value $\eta = 0.7$ for the determination of the IMF. Indeed, it is worth noting that there is a significant dispersion in the data (see Figure 4 of Tanaka et al. 2020) and a value $\eta = 0.5$ is well compatible for sizes $\lesssim$1 pc and is probably more physically justified. We will thus use $\eta = 0.5$ as the fiducial value for the velocity scale at the core scales in our calculations for the IMF. This well-established Burgers value for shock-dominated turbulence is confirmed by most observations in MCs (see, e.g., review by Hennebelle & Falgarone 2012). It should be noted that Henshaw et al. (2020) suggest a value $\eta = 0.37$ for the Brick. We have verified that using this value does not affect qualitatively our results, presented in Section 6.1. Note also that these observations rely on one single cloud in the CMZ, with a relatively low large-scale rms Mach number, namely $\mathcal{M} \simeq 11$ (Federrath et al. 2016). Therefore, the observations of the substructure in the

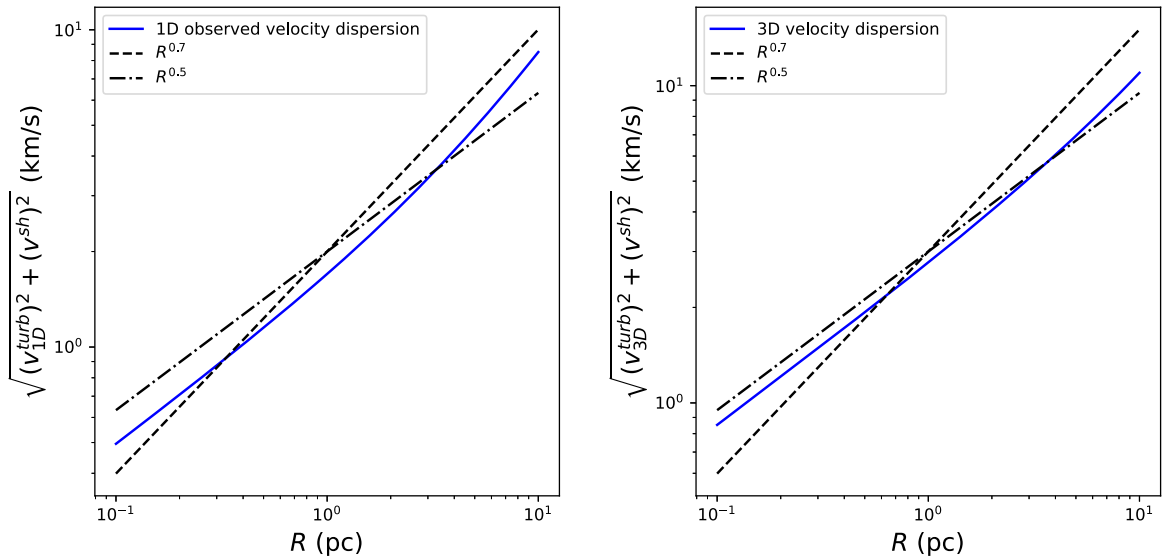

Figure 1. Top: 1D (observed); bottom: 3D total velocity dispersion.

Brick observed by Henshaw et al. (2020) are unlikely to be representative of the star-forming cloud population in the CMZ.

As shown in Appendix B, the collapse condition with the shear becomes (see Equation (B8))

$$e^{s_c} = \frac{2}{I}\frac{1}{\tilde{c}^2}\left[(1 + \mathcal{M}_\star^2 \tilde{a}^{2\eta}) + \left(\frac{3-\xi}{2}\right)^2 \frac{\mu}{3}\tilde{c}^2\right], \tag{30}$$

where $\mu = M(r_0)/\bar{\rho} r_0^3 \simeq 0.43$. The expression is similar to the one due to the tidal force (Equation (16)), but, in contrast to the latter, the shear always acts as a support to star formation, and it vanishes in case of solid-body rotation ($\xi = 3$), as expected. The reason is that the shear tears apart the gas accumulating in a given region, softening the local gravitational potential and thus allowing more gas to accumulate before collapsing eventually. As in the tidal case, we can estimate the impact of this support on the CMF. Using again $M \propto R^\gamma$ with $\gamma \simeq 2\eta + 1$ when the shear is negligible compared to the turbulence and $\gamma \to 3$ when $R \gg 1$, the dominant term in IMF scales as

$$\frac{dN}{d\log \tilde{M}_R} \propto \frac{de^{s_R^c}}{d\tilde{M}} \propto \tilde{M}^{-1-\frac{2}{\gamma}(1-\eta)}. \tag{31}$$

As γ varies from $2\eta + 1 \approx 2$ to 3, the slope varies from -1.25 to -1.2. The impact on the slope of the IMF due to the shear velocity dispersion is thus very small.

It should be mentioned that some studies have suggested that the impact of the shear on the dispersion velocity is comparable to the one due to turbulence (Federrath et al. 2016; Petkova et al. 2023). As mentioned previously, however, these studies suppose that the shear leads to a 3D dispersion velocity, whereas it should affect essentially 1D motions, yielding a smaller global impact.

5.2. The Shear as a Source of Deformation

The second effect of the shear is to distort the star-forming clump. The deformation of the semiaxis of a clump of size R due to the shear gradient during a typical turbulent timescale, assuming that the gas velocity is the shear velocity, can be estimated as (see Equation (B6))

$$\frac{a}{c} = 1 + 2\nabla v_r \tau_{\rm ct} \tag{32}$$

$$= 1 + 0.6\left(\frac{V_{\rm rms}}{V_0}\right)^{-1}\left(\frac{R}{1\ {\rm pc}}\right)^{0.3}, \tag{33}$$

where $\tau_{\rm ct} = R/V_{\rm rms}^{1D}$ is the typical turbulent crossing time at scale R and we have taken $V_0 = 2\ {\rm km\ s^{-1}}$ and $\eta = 0.7$ for the velocity–size relation for the cloud. This value is comparable to the one found in Krieger et al. (2020) and Tanaka et al. (2020), between 1.2 and 1.6. For a collapsing cloud, however, a more relevant timescale is the freefall time. Replacing $\tau_{\rm ct}$ by $\tau_{\rm ff}$ in the equation above, we get a value $\frac{a}{c} \approx 1.07$ for a 4 pc cloud like the Brick.

The correction due to the shear deformation on the collapsing barrier can be estimated by considering the integral of the deformation tensor (Chandrasekhar 1987), $I(a/c = 1.6, b/c = 1) \simeq 1.9$ and $I(a/c = 1.07, b/c = 1) \simeq 1.09$. The collapsing barrier is thus slightly increased because of the stabilizing effect of the ellipsoidal deformation.

Therefore, although the shear can have a substantial stabilizing effect for large-scale, noncollapsing clouds, it is negligible for small-scale collapsing ones.

The above two sections show that both the shear and the tides *slightly* affect the IMF slope of star-forming clumps in the CMZ (as a source of either deformation or velocity dispersion) within about the same order of magnitude, although with opposite contributions, yielding a global negligible effect. For the sake of completeness, we have examined in Appendix C the cumulative effect of tides and shear. In order to maximize the effects, we have considered ellipsoidal density fluctuations. The global result is that the collapsing barrier is found to be lower than the usual HC one. This was intuitively expected since, while the shear acts only in one dimension, the tides act in the three directions and thus dominate the global impact. However, the final result remains unchanged, as the global effect is found to be too small to explain the shallow IMF. It is worth pointing out that the results strongly depend on the chosen parameters at the cloud scale, b, V_0, and $\bar{n}$. The impact

on the CMF is maximized for a high velocity dispersion (typically 10 km s^{-1}) and low density $\bar{n} = 2 \times 10^3$ cm^{-3}. Such densities, however, seem to be inconsistent with the star-forming main cloud conditions observed in the CMZ.

6. The Dynamics of Star Formation in the CMZ

6.1. The Mass Function

There are observational suggestions that star formation in the CMZ does not occur continuously but through episodic starbursts (Yusef-Zadeh et al. 2009; Kruijssen et al. 2014; Henshaw et al. 2023). This is supported by numerical simulations that suggest bursts lasting about ∼5–10 Myr and separated by about ∼20–40 Myr, about the time for the clouds to migrate inward to the gravitationally unstable region at $R \sim 100$ pc (Krumholz & Kruijssen 2015; Krumholz et al. 2017), a process also found for other extragalactic nuclei (see review by Henshaw et al. 2023). The fact that the CMZ would be currently between two starbursts provides a plausible explanation for its particularly low SFR (see, e.g., Krumholz & Kruijssen 2015).

As shown, e.g., by Jeffreson et al. (2018), clouds are expected to collapse and form stars at radii from ∼45 to 100 pc, where shear is reduced and gas accumulates, while at short and large galactocentric distances the clouds are expected to be sheared apart before collapse and star formation occur, yielding low star formation efficiency (see, e.g., Krumholz & Kruijssen 2015; Jeffreson et al. 2018). Because of their high densities, these clouds have short lifetimes, ∼0.3–4 Myr (Kruijssen et al. 2015; Jeffreson et al. 2018). Interestingly enough, this corresponds to about one turbulence crossing time, $\tau_{\rm ct} \simeq L_c/V_{\rm rms}^{\rm 1D}$, for the clouds of interest, with $L_c \sim 1$–10 pc. Furthermore, given their short typical lifetimes compared with the timescale between two starburst episodes (see above), the clouds have experienced only one such episode before collapsing. In any case, the fact that $\tau_{\rm cloud} < \tau_{ct}$ implies that the cloud experiences only one turbulent episode during its lifetime. According to the Hennebelle–Chabrier time-dependent theory (Hennebelle & Chabrier 2011, 2013), the crossing time at the cloud scale is the typical time that is necessary for the density field generated by large-scale turbulence to be significantly modified, triggering a new set of density fluctuations, statistically independent of the former one. In strongly magnetized flows, as in the present case, the time required to rejuvenate a self-gravitating structure is even longer. Therefore, star formation within clouds in the CMZ should occur rapidly, throughout *one single episode of large-scale injection of turbulence*.

In that case, the static, time-independent approach of the HC theory should be used instead of the time-dependent one. Indeed, in the latter case, small-scale density fluctuations can keep collapsing during the collapse of large ones (which have a longer freefall timescale) because turbulence is constantly replenished at the the cloud scale during the cloud lifetime ($\tau_{\rm ct} < \tau_{\rm ff}^0$). In contrast, for the CMZ conditions, the above estimate shows that the cloud has collapsed before the first episode of turbulence has had time to dissipate and a new one will be generated at large scales.

As shown in HC13, the time-independent description of the IMF yields a shallower IMF than the time-dependent one, by a factor $\Delta\alpha = (\eta - 1)/(2\eta + 1)$ (see their Equations (24) and (25)). This is illustrated in the left panel of Figure 2. While the time-dependent derivation yields a too-steep high-mass tail for the IMF, the time-independent formulation properly reproduces the observed value. We stress the fact that there is no adjustable parameter in this theory. It is just applied in the present context to the characteristic properties of the CMZ star-forming clouds (Section 2). In order to verify this result, we have carried out the same type of calculations with the Hopkins (2012) excursion set formalism (long-dashed line in Figure 2). As seen in the figure, the result is confirmed.

It is worth noting that, as seen in the figure, not only does the time-dependent calculation fail to reproduce the correct value for the Arches cluster, but it does not even recover the Salpeter value. This seems to be at odds with Figures 1 and 2 of HC13, which show that, for standard MW clouds, the time-dependent theory yields the correct slope. The key point is that while usual Larson MW conditions correspond to $\mathcal{M}_\star \simeq \sqrt{2}$, the present ones give $\mathcal{M}_\star \simeq 10$ for the velocity dispersion appropriate to the core scales (Tanaka et al. 2020; see Section 3.1). As shown in HC08 (their Figure 1), the larger $\mathcal{M}_\star$ is, the shallower the high-mass slope, a consequence of the more vigorous turbulence cascade. Such levels of turbulence are reached in massive early-type galaxies, even though the proper slope of the IMF is recovered with the time-dependent HC theory (Chabrier et al. 2014). These galaxies, however, are at least 10 times denser than in the present case (see Table 1 of Chabrier et al. 2014), increasing the role of gravity to counteract the one of turbulence in the collapse process. This confirms the fact that, for typical density–turbulence conditions in CMZ star-forming clouds, an ongoing injection process of large-scale turbulence cannot produce the observed high-mass slope, in contrast to the "one single turbulence injection episode" scenario.

For the sake of completeness, we also show in the right panel of Figure 2 the IMF obtained in the time-independent case if the pdf of the cloud is modified by the strong magnetic field for the (unlikely) case $B \propto \bar{n}^{1/2}$, as discussed in Section 3.3. We have used the more appropriate velocity dispersion value of Tanaka et al. (2020) for the cores (see discussion in Section 3.2). In that case, the high-mass slope of the CMF is flattened and becomes consistent with the observed value. However, such a field–density amplification is unlikely to occur for CMZ cloud densities. Indeed, the magnetic field is usually found to saturate at densities $\lesssim 10^4$ cm^{-3} (e.g., Hu & Lazarian 2023). As discussed in Section 3.3, in that case the magnetic field plays no role in the gas pdf.

As shown in HC08, the transition from the large-scale turbulence-dominated regime to the small-scale thermal one corresponds to a mass $\tilde{M} \simeq 2(\mathcal{M}_\star)^{-1/\eta} \approx 0.02$ under the present conditions against $\sim 0.8\, M_\odot$ for usual cloud conditions (see Equation (45) of HC08). Therefore, whereas for usual MW conditions the peak of the IMF ($d\mathcal{N}/d\tilde{M} = 0$) occurs in the thermal regime, under the present conditions it occurs in the *turbulence-dominated* one, as shown in Figure 2. From the physical point of view, this means that under CMZ cloud conditions the vigorous turbulence can generate and prevent from collapsing a larger number of density fluctuations than under usual conditions. Note also that the warmer gas provides a larger thermal support. We stress again that, as explained in detail in Chabrier & Hennebelle (2011), the role of turbulence in the HC theory of the IMF should *not* be considered in a static (pressure-like) sense because turbulence has already dissipated by the time the prestellar core is formed. Turbulence in the HC

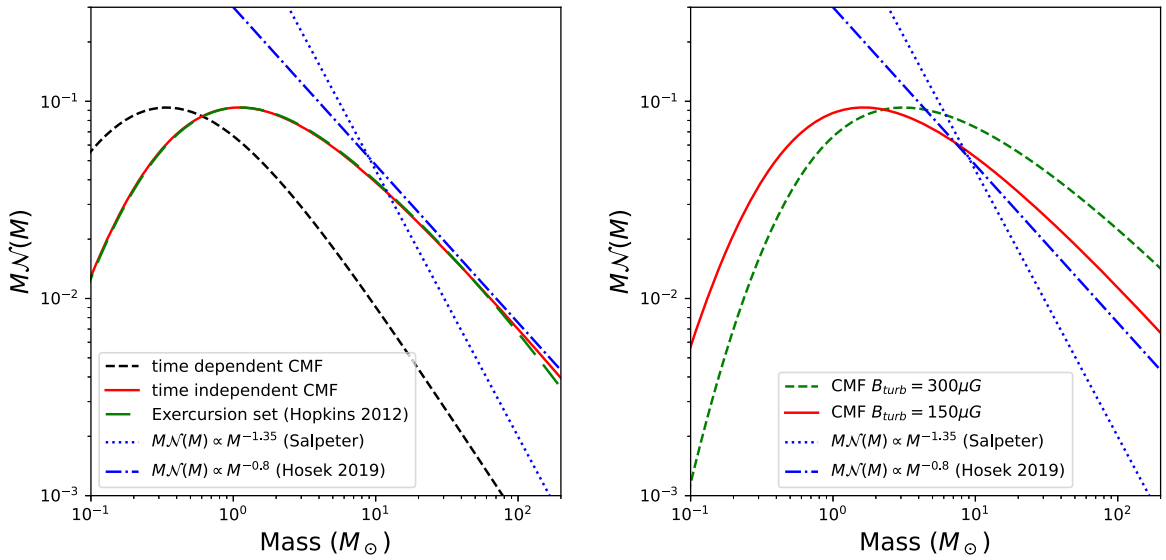

Figure 2. Left: IMF $dN/d\log M$ calculated with the time-dependent (HC13; short-dashed line) and time-independent (HC08; solid line) Hennebelle–Chabrier theory for a magnetized cloud of size $L_c = 10$ pc with no impact of the magnetic field on the pdf (B$\propto n^0$). Long-dashed line: time-independent IMF calculated with the Hopkins (2012) excursion set formalism; dotted line: Salpeter IMF; dashed–dotted line: IMF observed for the Arches Hosek et al. (2019). Right: IMF calculated with the time-independent (HC08) theory for two representative values of the turbulent magnetic field from Lu et al. (2024) taking into account the modification of the variance of the pdf (Equation (6)), which corresponds to $\beta = 0.25$ and 1, respectively. This supposes a field–density dependence $B \propto n^{1/2}$, and we have taken the velocity normalization of Tanaka et al. (2020).

sense must be understood as a dynamical, statistical process, turbulence generating *at the very initial stages* a field of density fluctuations and sweeping away the ones not dense enough to have a chance to collapse under the action of gravity, allowing more gas to accumulate locally before becoming gravitationally unstable. By the time a dense enough fluctuation has started to collapse into a prestellar core, the turbulence at the core scale has dissipated and has become transonic or subsonic. What matters in this formalism is thus the turbulence *rms velocity* rather than pressure.

6.2. The Source of Turbulence

Various sources of turbulence driving in the CMZ have been examined in Kruijssen et al. (2014) and Henshaw et al. (2023). Among different processes, these authors found that bar inflow could explain the observed turbulent energy. This is confirmed in a study by Sormani & Barnes (2019), who find that gas inflow is a promising candidate for driving the turbulence in the CMZ. It is indeed well-known that the bar transports matter and energy radially from the Galactic disk to the CMZ (see, e.g., Krumholz & Kruijssen 2015; Portail et al. 2017). Mass transport is a natural consequence of the disk instability, as the strongly nonaxisymmetric structure of the Galactic bar exerts torques that tend to drive angular momentum out and thus yield inward mass transport by angular momentum conservation. When mass is transported inward through the disk and down the overall potential well, part of the gravitational energy gain can be converted into turbulence (see, e.g., Wada et al. 2002). Shear stress, notably near the boundary between the (inner) gravitationally dominated region and (outer) shear-dominated region of the CMZ, will also contribute to turbulent driving at large scales. On the other hand, estimates of energy injected by supernovae in the CMZ, after a first generation of stars has been formed, are also found potentially to contribute significantly to turbulence in the CMZ (Henshaw et al. 2023). This list, of course, is not exhaustive, and processes like acoustic or MRI disk instabilities might also contribute to the turbulence driving, even though it seems difficult for these processes alone to sustain the observed high levels of turbulence (Henshaw et al. 2023). All these processes, at different levels, constantly drive high levels of velocity dispersion in the CMZ. This provides the seed for the generation of density fluctuations, once enough gas has accumulated again in the potential dominated region, after the leftover gas due to the previous star formation episode has been dispersed. This will provide the turbulent dense gas reservoir necessary to generate a new field of density fluctuations, eventually yielding a new starburst episode. Interestingly enough, note that 30–40 Myr, the expected duration of the quiescent phase, is about the lifetime of a 8 $M_\odot$ star, the smallest mass for Type II supernova progenitors, before it explodes as a supernova. During this period, supernova explosions will at the very least slow down the inward gas inflow. This provides a support, besides the aforementioned inward gas migration argument, for the duration of the quiescent phase. Furthermore, as mentioned by Krumholz & Kruijssen (2015), "quiescent" does not necessarily mean that the gas is completely depleted, but rather that it is driven out of a self-gravitating state.

6.3. The Star Formation Rate

The fact that star formation occurs within one single turbulent episode will also reduce the SFR. Indeed, once a fluctuation of scale R has collapsed, it will not be rejuvenated by a new episode of turbulence cascade dissipation. In that case, the derivation of the SFR per freefall time yields (see HC13)

$$\mathrm{SFR}_{\mathrm{ff}}^{0} = \int_0^{M_{\mathrm{cut}}} \frac{M\mathcal{N}(M)}{\bar{\rho}} dM \tag{34}$$

$$= \int_{\tilde{\rho}_{\mathrm{cut}}}^{+\infty} \mathcal{P}(\tilde{\rho}) d\tilde{\rho} \tag{35}$$

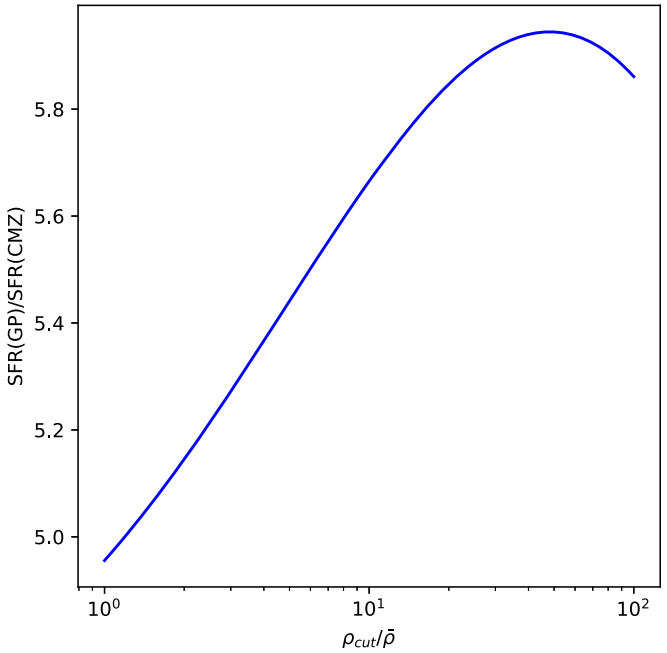

Figure 3. Ratio of the SFR in the Galactic plane (GP) and in the CMZ from the HC13 model as a function of $\tilde{\rho}_{\rm cut}$. The SFR in the CMZ is calculated from the time-independent model (Equation (36)) with parameters characteristic of the CMZ. The SFR in the GP is calculated from the time-dependent model from HC13 with parameters characteristic of the GP.

$$= \frac{1}{2}\left(\mathrm{erf}\left(\frac{\sigma^2 - 2\log(\tilde{\rho}_{\rm cut})}{2^{3/2}\sigma}\right) + 1\right), \tag{36}$$

where $\tilde{\rho} = \rho/\bar{\rho}$ and we assume that the probability distribution depends weakly on scale R. As in HC13, we take $y_{\rm cut} = \tilde{R}_{\rm cut}/\tilde{L}_c \simeq 0.1 - 0.3$, which corresponds to

$$\tilde{\rho}_{\rm cut} = \frac{1 + \mathcal{M}_\star^2 \tilde{R}_{\rm cut}^{2\eta}}{\tilde{R}_c^2} \simeq 4 - 14. \tag{37}$$

Compared with Equation (45) of Hennebelle & Chabrier (2011), we notice the absence of the prefactor $e^{(3\sigma^2/8)}$, which stems from the disappearance of the density freefall timescale $\tilde{\rho}^{1/2}$ in the integral.

Figure 3 compares the SFR predicted by the usual time-dependent HC theory for fiducial MC conditions ($\mathcal{M} = 15$, $b = 0.5 \Rightarrow \sigma \simeq 2$) with the SFR typical of CMZ conditions ($\mathcal{M} = 100$, $b = 0.3 \Rightarrow \sigma \simeq 2.6$). We see that assuming that star formation in CMZ MCs occurs throughout one single episode of turbulence injection at the cloud scale reduces the SFR by about a factor 5–6. As shown in Figure 3, this ratio depends very weakly on the choice of $y_{\rm cut}$.

A point worth mentioning is that feedback has often been suggested as an explanation to reduce the SFR in the CMZ. At least dynamical feedback, however, is already implicitly taken into account in the stronger-than-usual velocity dispersion and in the modified index n of turbulence through the Larson parameter η. Indeed, as shown in HC08 (their Equation (24)), both indexes are related through the relation $\eta = (n-3)/2$. The observed value $\eta = 0.7$ thus implies an index of turbulence $n = 4.4$, larger than the Burgers value. It seems thus reasonable to suggest that the shear and the dynamical feedback are the reasons for such a modification of the velocity dispersion relation in the CMZ. Distinguishing between the turbulence and shear contributions, however, is generally not done in the observational analysis.

Some simulations have pointed out the shear for lowering the SFR both in the solar neighborhood (Colling et al. 2018) and in the CMZ (Emsellem et al. 2015; Dale et al. 2019; Li & Zhang 2020), even though Dib et al. (2012) show that the impact of the shear on the SFR is not relevant far from the GC. This seems to be in contradiction with the analysis carried out in Section 5.

These studies, however, consider a much less dense medium (or much larger clouds) than the one characteristic of the CMZ, although with a strong shear. As shown in Section 5, the more diluted the medium, the greater the impact of the shear. Similarly, Federrath et al. (2016) have suggested that turbulent velocity dispersion, density, and forcing parameter like the ones observed in the Brick cloud and used in Kruijssen et al. (2019) lead to the right SFR. However, as mentioned in Section 5, these authors assume in their analysis that the shear acts in the three directions. Taking a more reasonable assumption of a 1D action of the shear, we have shown that its effect is much more modest in the region of the star-forming clouds.

7. Conclusion

In this paper, we have examined various physical processes that may explain the shallow high-mass slope of the IMF, as well as the low SFR in star-forming MCs in the CMZ. We show that neither the strong tidal field nor the Galactic shear experienced by the CMZ can explain these unusual properties, *in the molecular gas region where star-forming clouds form*. Both effects have a negligible impact in this region. Moreover, interestingly enough, shear and tidal interactions have opposite effects. While tides lower the collapsing barrier, promoting the collapse of overdense fluctuations, the shear increases the barrier, bringing support against collapse. Both effects are similar and nearly compensate. Similarly, we show that the intense magnetic field in the CMZ provides a negligible pressure support and does not modify the pdf of the turbulent gas flow in the clouds, *except if it does not saturate and keeps being amplified at these high densities*. This hypothesis lacks a robust physical explanation and is thus unlikely.

In contrast, we show that, contrary to the case of MCs in the Galactic disk, clouds in the CMZ experience only one single episode of turbulence injection at large scales, most likely due to bar instabilities and radial mass transport (see Section 6.2). Indeed, their rather short lifetime, due to their high mean densities, is similar to one typical turbulence crossing time at the injection (i.e., cloud) scale. Consequently, according to the Hennebelle–Chabrier theory of star formation, within this "single turbulence episode" scenario, the cloud experiences one single field of turbulence-induced density fluctuations, leading eventually to gravitationally unstable prestellar cores. New generations of large-scale turbulence-induced density fluctuations have no time to occur. As shown in Hennebelle & Chabrier (2013), for a given cloud mass, this yields a flatter IMF than usual, leading to the correct observed value for the characteristics of the CMZ star-forming clouds. We also suggest that the severe steepening observed in the IMF of the Arches cluster, with an age of ∼2–4 Myr, above $\sim 40\,M_\odot$ (Hosek et al. 2019) can be explained by the maximum lifetime of these stars before they explode as supernovae. More massive stars have already exploded as supernovae.

Furthermore, this single large-scale turbulence event within the cloud lifetime yields by itself a 5–6 times lower SFR than under usual MW cloud conditions, again in agreement with the observed values. Therefore, we conclude that our "single large-scale turbulence injection" scenario for CMZ star-forming clouds provides a plausible, consistent explanation for both the observed shallow high-mass slope and the low SFR in the CMZ.

Appendix A
Tidal Tensor and Virial Collapse Condition

We consider an MC whose center of mass m_0 is at a distance r_0 from the GC. We also consider a mass $m_1 \ll m_0$ located in the MC at the position $\boldsymbol{r}$ from its mass center and at $\boldsymbol{r}_1 = \boldsymbol{r}_0 + \boldsymbol{r}$ from the GC. The mass in the CMZ creates an axisymmetric gravitational field ϕ. The tidal force on m_1 is the difference between the force exerted on m_1 and the one exerted on the center of mass of the system $\{m_0 + m_1\}$:

$$\boldsymbol{F}_t = -m_1[\boldsymbol{\nabla}\phi(\boldsymbol{r}_0 + \boldsymbol{r}) - \boldsymbol{\nabla}\phi(\boldsymbol{r}_0)]. \tag{A1}$$

As the mass of the cloud is very small compared with the one generating the tidal field, we neglect its gravitational field. A Taylor expansion in the Cartesian frame $\boldsymbol{e}_x$, $\boldsymbol{e}_y$, $\boldsymbol{e}_z$ (as in Dale et al. 2019), $\boldsymbol{e}_x \| \boldsymbol{r}_0$, yields

$$F_t^j(\boldsymbol{r}) = -m_1 r_k \frac{\partial \phi}{\partial x_k \partial x_j}(\boldsymbol{r}). \tag{A2}$$

The tidal term involved in the virial theorem is given by

$$T_{ii} = \int \rho \boldsymbol{f}_t^i \, r_i dV \simeq -\int \rho \frac{\partial \phi}{\partial r_i^2} r_i^2 dV, \tag{A3}$$

where $r_i = x$, y, or z and $\boldsymbol{f}_t = \boldsymbol{F}_t/m_1$ is the tidal force by unit of mass. Note that in the last equality we neglected the nondiagonal terms of Equation (A2) because they correspond to negligible corrections. The system of coordinates used here is summarized in Figure 4. In the cylindrical frame associated with the GC, the radial gravitational field is given by

$$\boldsymbol{G}(r) = -\frac{GM(r)}{r^2}\boldsymbol{e}_r \Leftrightarrow \phi(r) = \frac{GM(r)}{(\xi - 1)r}, \tag{A4}$$

where $M(r) \propto r^{\xi}$ is the mass enclosed within a radius r, with $\xi = 2.2$ the value determined from the gravitational potential of the CMZ (Launhardt et al. 2002; Kruijssen et al. 2015; solid-body rotation corresponds to $\xi = 3$). Using $dr/dy = y/r_0$ and considering the flattening of the gravitational field along the z-axis (Dale et al. 2019), we deduce the three diagonal components of the tensor:

$$\frac{\partial^2\phi}{\partial x^2} = (\xi - 2)\frac{GM(r)}{r^3}; \frac{\partial^2\phi}{\partial y^2} = \frac{GM(r)}{r^3}; \frac{\partial^2\phi}{\partial z^2} = \frac{GM(r)}{q_\phi^2 r^3}, \tag{A5}$$

where q_ϕ produces a potential flattened in the z-direction. As $\xi > 2$, all components of the tidal tensor are compressive. Doing the usual change of variable between Cartesian and spherical coordinates for an ellipsoid yields for the components of the tidal tensor

$$T_{xx} = \frac{2 - \xi}{5} M_c c^2 \frac{GM(r_0)}{r_0^3}, \tag{A6}$$

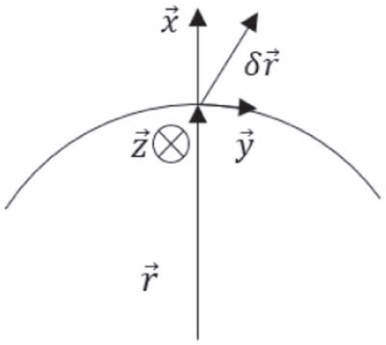

Figure 4. Reference frame for the calculation of the tides and the shear.

$$T_{yy} = -\frac{1}{5} M_c b^2 \frac{GM(r_0)}{r_0^3}, \tag{A7}$$

$$T_{zz} = -\frac{1}{5} M_c c^2 \frac{GM(r_0)}{q_\phi^2 r_0^3}, \tag{A8}$$

where M_c is the total mass of the studied MC and a, b, and c are the three lengths of the ellipsoid.

An equation of motion can be written for each axis:

$$\frac{1}{2}\frac{\partial^2 I_{ii}}{\partial t^2} = PV + 2K_{ii} + W_{ii} + T_{ii}, \tag{A9}$$

where I_{ii}, K_{ii}, W_{ii}, and T_{ii} denote, respectively, the inertial, kinetic, gravitational, and tidal tensors. Denoting $\tilde{x}$ the quantities normalized to the Jeans length, $\lambda_{\rm J} = C_s/\sqrt{\bar{\rho}G}$, Jeans mass, $M_{\rm J} = 4\pi/3\bar{\rho}\lambda_{\rm J}^3$, and mean freefall time, $\tau = 1/\sqrt{G\bar{\rho}}$, one gets after calculations

$$\begin{aligned}
\frac{1}{2}\frac{\partial^2\tilde{c}^2}{\partial\tilde{t}^2} &= \frac{5}{2}(1 + \mathcal{M}_\star^2\tilde{a}^{2\eta}) - \pi\alpha_1\tilde{c}^2 e^s - \frac{\xi - 2}{2}\tilde{c}^2\mu, \\
\frac{1}{2}\frac{\partial^2\tilde{b}^2}{\partial\tilde{t}^2} &= \frac{5}{2}(1 + \mathcal{M}_\star^2\tilde{a}^{2\eta}) - \pi\alpha_2\tilde{c}^2 e^s - \frac{1}{2}\tilde{b}^2\mu, \\
\frac{1}{2}\frac{\partial^2\tilde{a}^2}{\partial\tilde{t}^2} &= \frac{5}{2}(1 + \mathcal{M}_\star^2\tilde{a}^{2\eta}) - \pi\alpha_3\tilde{c}^2 e^s - \frac{1}{2q_\phi^2}\tilde{a}^2\mu,
\end{aligned} \tag{A10}$$

with $\mu = M(r_0)/\bar{\rho}r_0^3 \simeq 0.08$ and $q_\phi = 0.63$ (Dale et al. 2019). For the sake of simplicity, we neglect the possible modification of turbulence by accretion on or dissipation of the cloud and thus replace $a^{2\eta}$ by $a(t=0)^{2\eta}$, where a is the longest length of the cloud.

Following the Hennebelle–Chabrier formalism, the global collapse condition is obtained be summing these three equations:

$$\begin{aligned}
e^{s_c} = \frac{\rho_R^c}{\bar{\rho}} = \frac{2}{I}\frac{1}{\tilde{c}^2}\Bigg[(1 + \mathcal{M}_\star^2\tilde{a}^{2\eta}) - \frac{\mu}{15}\tilde{c}^2((\xi - 2) \\
+ \frac{\tilde{b}^2}{\tilde{c}^2} + \frac{\tilde{a}^2}{q_\phi^2\tilde{c}^2})\Bigg],
\end{aligned} \tag{A11}$$

where $I(a, b, c) = \int_0^\infty \frac{du}{\sqrt{\left(1 + \left(\frac{c}{a}\right)^2 u\right)\left(1 + \left(\frac{c}{b}\right)^2 u\right)(1 + u)}}$ (Chandrasekhar 1987). The first term in the brackets is the usual HC08 barrier, while the second term is the tidal contribution.

Appendix B
Shear

We consider a rotating frame of angular velocity Ω associated with the center of mass of a cloud located at a distance r from the GC. Using the usual transformations for time derivatives between the rotation and inertial frames (at the GC), we deduce the relation at any point of the cloud:

$$\boldsymbol{v}_r(\boldsymbol{r}+\delta\boldsymbol{r}) = \boldsymbol{v}_i(\boldsymbol{r}+\delta\boldsymbol{r}) - \boldsymbol{\Omega}(r)\times(\boldsymbol{r}+\delta\boldsymbol{r}), \tag{B1}$$

where $\delta\boldsymbol{r} = x\,\boldsymbol{e}_x + y\,\boldsymbol{e}_y$ in the rotating basis, $\boldsymbol{\Omega} = \Omega\,\boldsymbol{e}_z$, and $\boldsymbol{v}_i = \boldsymbol{\Omega}(\boldsymbol{r}+\delta\boldsymbol{r})\times(\boldsymbol{r}+\delta\boldsymbol{r})$. Thus,

$$\begin{aligned}\boldsymbol{v}_r &= (\boldsymbol{r}+\delta\boldsymbol{r})\times(\boldsymbol{\Omega}(\boldsymbol{r}+\delta\boldsymbol{r}) - \Omega(\boldsymbol{r}))\\ &= (\boldsymbol{r}+\delta\boldsymbol{r})\times[(\delta\boldsymbol{r}\cdot\boldsymbol{\nabla})\boldsymbol{\Omega}(\boldsymbol{r})].\end{aligned} \tag{B2}$$

We define the axis orientation illustrated in Figure 4. We thus have

$$r_1 = |\boldsymbol{r}+\delta\boldsymbol{r}| = r\sqrt{1+\frac{x^2+y^2}{r^2}+2\frac{x}{r}}. \tag{B3}$$

At first order, we deduce $r_1 = r + x$. Then, using this expression, we have

$$\boldsymbol{v}_r = -(\boldsymbol{r}+\delta\boldsymbol{r})\times x\frac{d\Omega}{dr}\boldsymbol{e}_z = -rx\frac{d\Omega}{dr}\boldsymbol{e}_y. \tag{B4}$$

The minus sign comes from the fact that $\boldsymbol{\Omega}$ is oriented in the direction opposite to $\boldsymbol{e}_z$. To compare with the conditions used in simulations (Dale et al. 2019; Kruijssen et al. 2019), we give the numerical value of the velocity gradient:

$$\begin{aligned}\nabla v_r = r\frac{d\Omega}{dr} &= \frac{3-\xi}{2}\sqrt{\frac{GM(r)}{r^3}}\\ &\simeq 1\times10^{-14}\ \mathrm{s^{-1}} \simeq 0.7\ \mathrm{Myr^{-1}} \simeq 700\ \mathrm{km\ s^{-1}\,kpc^{-1}},\end{aligned} \tag{B5}$$

where $\xi = 2.2$ is the coefficient of the mass distribution $M(r)\propto r^{\xi}$ determined from the gravitational potential of the CMZ, with $M = 5\times10^8\ M_\odot$ at $r = 90$ pc (Kruijssen et al. 2019). This value is larger than the one used by Colling et al. (2018); this is due to the fact that in these simulations they are far from the GC. At first order, the velocity dispersion only exists along the y-axis, but at second order there is also an effect along the x-axis, as emphasized by Kruijssen et al. (2019, see their Table 3). In the rotational frame, the velocity dispersion at scale R is thus

$$v_r = \nabla v_r\, r \simeq 0.7\left(\frac{R}{1\ \mathrm{pc}}\right)\mathrm{km\ s^{-1}}, \tag{B6}$$

which is smaller by at least a factor of 3 than the turbulent velocity dispersion (see Section 2). The associated energy per unit mass can be estimated as

$$\frac{1}{2}v_r^2 = \frac{1}{2}\left(\frac{3-\xi}{2}\right)^2\frac{GM(r)}{r^3}R^2. \tag{B7}$$

The collapsing barrier in HC08 thus becomes

$$e^{s_c} = \frac{2}{I}\frac{1}{\tilde{c}^2}\left[(1+\mathcal{M}_\star^2\tilde{a}^{2\eta}) + \left(\frac{3-\xi}{2}\right)^2\frac{\mu}{3}\tilde{c}^2\right], \tag{B8}$$

where $\mu = M(r_0)/\bar{\rho}r_0^3 \simeq 0.08$.

Appendix C
The Cumulative Role of Shear and Tides in the Stability of an Ellipsoidal Deformable Perturbation

In the global energy budget of the perturbation, the shear is dominated by the tides because the latter act in three directions while the shear applies only on one axis. In order to quantify the global effect, we solve the complete system of the three virial equations accounting for both shear and tides. Starting from Equation (A10) and adding a velocity dispersion coming from the shear along one of the axes (here the axis c, the one for which the shear is the strongest relative to the tides), we have

$$\begin{aligned}\frac{1}{2}\frac{\partial^2\tilde{c}^2}{\partial\tilde{t}^2} &= \frac{5}{2}(1+\mathcal{M}_\star^2\tilde{a}^{2\eta})\\ &-\pi\alpha_1\tilde{c}^2e^s - \frac{\xi-2}{2}\tilde{c}^2\mu,\\ \frac{1}{2}\frac{\partial^2\tilde{b}^2}{\partial\tilde{t}^2} &= \frac{5}{2}(1+\mathcal{M}_\star^2\tilde{a}^{2\eta}) - \pi\alpha_2\tilde{c}^2e^s - \frac{1}{2}\tilde{b}^2\mu\\ &+\frac{5}{2}\left(\frac{3-\xi}{2}\right)^2\mu\tilde{c}^2,\\ \frac{1}{2}\frac{\partial^2\tilde{a}^2}{\partial\tilde{t}^2} &= \frac{5}{2}(1+\mathcal{M}_\star^2\tilde{a}^{2\eta}) - \pi\alpha_3\tilde{c}^2e^s - \frac{1}{2q_\phi^2}\tilde{a}^2\mu,\end{aligned} \tag{C1}$$

where $\mu = M_0/(r_0^3\bar{\rho})$ is the mass enclosed within a galactocentric radius $r_0 = 100$ pc, $M(r) = r^{\xi}$ with $\xi = 2.2$, as inferred from the galactic density profile. By comparing the tidal terms and the shear term, we notice that the support from both the shear and the tides increases when $\xi\to0$ ($\xi\ll3$), i.e., when the density quickly decreases. Note that the shear supports tangentially the cloud, explaining why the shear term enters in the equation of evolution of the axis b.

In the case $\xi = 2.2$, we have the equality

$$\frac{5}{2}\left(\frac{3-\xi}{2}\right)^2 - \frac{1}{2} = -\frac{\xi-2}{2} < 0. \tag{C2}$$

The evolution of the axes b and c will thus be the same, and the three axes will collapse if the initial density is the one given by the HC08 critical density in spite of the support of the shear. This confirms that the shear is dominated by the tides. This is illustrated in Figure 5.

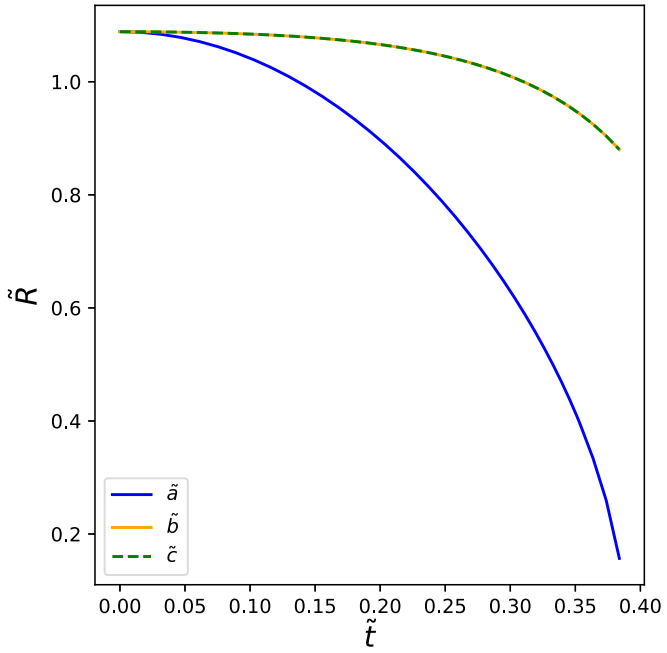

Figure 5. Evolution of the three axes of a 1 pc initially spherical density perturbation formed in a turbulence flow injected at 10 pc. The initial density is the HC08 critical density, so in absence of tides and shear, the axis will not evolve. The turbulent velocity normalization is the one observed by Krieger et al. (2020). The time (x-axis) is normalized to the freefall time, and the length (y-axis) is normalized to the Jeans length at the injection scale. The shear slows down the collapse but is unable to prevent it.

ORCID iDs

Gilles Chabrier https://orcid.org/0000-0002-8342-9149

References

Andersen, M., Barnes, P. J., Tan, J. C., Kainulainen, J., & de Marchi, G. 2017, ApJ, 850, 12
Beresnyak, A., Lazarian, A., & Cho, J. 2005, ApJL, 624, L93
Chabrier, G., & Hennebelle, P. 2011, A&A, 534, A106
Chabrier, G., Hennebelle, P., & Charlot, S. 2014, ApJ, 796, 75
Chandrasekhar, S. 1987, Ellipsoidal Figures of Equilibrium (New York: Dover)
Colling, C., Hennebelle, P., Geen, S., Iffrig, O., & Bournaud, F. 2018, A&A, 620, A21
Dale, J. E., Kruijssen, J. M. D., & Longmore, S. N. 2019, MNRAS, 486, 3307
Dib, S., Helou, G., Moore, T. J. T., Urquhart, J. S., & Dariush, A. 2012, ApJ, 758, 125
Dib, S., Kim, J., & Shadmehri, M. 2007, MNRAS, 381, L40
Emsellem, E., Renaud, F., Bournaud, F., et al. 2015, MNRAS, 446, 2468
Federrath, C., Rathborne, J. M., Longmore, S. N., et al. 2016, ApJ, 832, 143
Hennebelle, P., & Chabrier, G. 2008, ApJ, 684, 395
Hennebelle, P., & Chabrier, G. 2011, ApJL, 743, L29
Hennebelle, P., & Chabrier, G. 2013, ApJ, 770, 150
Hennebelle, P., & Falgarone, E. 2012, A&ARv, 20, 55
Henshaw, J. D., Barnes, A. T., Battersby, C., et al. 2023, in ASP Conf. Ser. 534, Protostars and Planets VII, ed. S. Inutsuka et al. (San Francisco, CA: ASP), 83
Henshaw, J. D., Ginsburg, A., Haworth, T. J., et al. 2019, MNRAS, 485, 2457
Henshaw, J. D., Kruijssen, J. M. D., Longmore, S. N., et al. 2020, NatAs, 4, 1064
Hopkins, P. F. 2012, MNRAS, 423, 2037
Hosek, M. W. J., Lu, J. R., Anderson, J., et al. 2019, ApJ, 870, 44
Hu, Y., & Lazarian, A. 2023, MNRAS, 524, 4431
Hußmann, B., Stolte, A., Brandner, W., Gennaro, M., & Liermann, A. 2012, A&A, 540, A57
Jaupart, E., & Chabrier, G. 2020, ApJ, 903, L2
Jeffreson, S. M. R., Kruijssen, J. M. D., Krumholz, M. R., & Longmore, S. N. 2018, MNRAS, 478, 3380
Krieger, N., Bolatto, A. D., Koch, E. W., et al. 2020, ApJ, 899, 158
Kruijssen, J. M. D., Dale, J. E., & Longmore, S. N. 2015, MNRAS, 447, 1059
Kruijssen, J. M. D., Dale, J. E., Longmore, S. N., et al. 2019, MNRAS, 484, 5734
Kruijssen, J. M. D., & Longmore, S. N. 2013, MNRAS, 435, 2598
Kruijssen, J. M. D., Longmore, S. N., Elmegreen, B. G., et al. 2014, MNRAS, 440, 3370
Krumholz, M. R., & Kruijssen, J. M. D. 2015, MNRAS, 453, 739
Krumholz, M. R., Kruijssen, J. M. D., & Crocker, R. M. 2017, MNRAS, 466, 1213
Lada, C. J., Forbrich, J., Lombardi, M., & Alves, J. F. 2012, ApJ, 745, 190
Launhardt, R., Zylka, R., & Mezger, P. G. 2002, A&A, 384, 112
Li, G.-X., & Zhang, C.-P. 2020, ApJ, 897, 89
Lim, B., Chun, M.-Y., Sung, H., et al. 2013, AJ, 145, 46
Lohr, M. E., Clark, J. S., Najarro, F., et al. 2018, A&A, 617, A66
Longmore, S. N., Bally, J., Testi, L., et al. 2013, MNRAS, 429, 987
Lu, J. R., Do, T., Ghez, A. M., et al. 2013, ApJ, 764, 155
Lu, X., Cheng, Y., Ginsburg, A., et al. 2020, ApJL, 894, L14
Lu, X., Liu, J., Pillai, T., et al. 2024, ApJ, 962, 39
Molina, F. Z., Glover, S. C. O., Federrath, C., & Klessen, R. S. 2012, MNRAS, 423, 2680
Padoan, P., & Nordlund, Å. 2002, ApJ, 576, 870
Padoan, P., Nordlund, A., & Jones, B. J. T. 1997, MNRAS, 288, 145
Pang, X., Grebel, E. K., Allison, R. J., et al. 2013, ApJ, 764, 73
Petkova, M. A., Kruijssen, J. M. D., Henshaw, J. D., et al. 2023, MNRAS, 525, 962
Portail, M., Gerhard, O., Wegg, C., & Ness, M. 2017, MNRAS, 465, 1621
Schneider, N., Ossenkopf-Okada, V., Clarke, S., et al. 2022, A&A, 666, A165
Sormani, M. C., & Barnes, A. T. 2019, MNRAS, 484, 1213
Tanaka, K., Nagai, M., Kamegai, K., Iino, T., & Sakai, T. 2020, ApJ, 903, 111
Wada, K., Meurer, G., & Norman, C. A. 2002, ApJ, 577, 197
Yusef-Zadeh, F., Hewitt, J. W., Arendt, R. G., et al. 2009, ApJ, 702, 178